communications chemistry

A Nature Portfolio journal

Article

https://doi.org/10.1038/s42004-025-01529-8

Axial chirality-induced rigidification in aminoboranes enhances persistent room-temperature phosphorescence and circularly polarized luminescence

Jusaina Eyyathiyil [1], Subhajit Ghosh [1], Arunima Cheran [2], Silvano Geremia [3], Jatish Kumar [2] ✉, Neal Hickey [3] ✉ & Pakkirisamy Thilagar [1] ✉

Long-lived triplet exciton harvesting materials are of immense interest for applications in bioimaging, optoelectronics, anticounterfeiting, and sensing. However, achieving persistent room-temperature phosphorescence (pRTP) in metal-free systems remains a significant challenge. Herein, we present purely organic axially chiral aminoboranes (***R/S*-(BN)$_2$**) with enhanced pRTP properties and circularly polarized luminescence (CPL). By introducing axial chirality, the dual-core (***R/S*-(BN)$_2$**) system achieves steric-hindrance-caused rigidity, which restricts molecular motions, leading to superior phosphorescence properties. Notably, ***R*-(BN)$_2$** demonstrates a phosphorescence quantum yield (Φ_P) of 9.2% (***S*-(BN)$_2$** : Φ_P = 8.7%) and an extended lifetime of 0.9 sec at room temperature, significantly outperforming its mono-core counterpart **(BN)$_1$** (Φ_P = 3.0% and τ_P = 0.6 s). Theoretical analysis corroborates the observed improvements, revealing the synergistic role of borylation and axial chirality in stabilizing triplet states. Furthermore, the axially chiral aminoboranes exhibited CPL in dichloromethane solutions with a dissymmetry factor of ~10^{-3}. These findings highlight the potential of axially chiral frameworks in designing efficient metal-free pRTP materials, as demonstrated in the security writing application, further paving the way for their use in bioimaging, anti-counterfeiting technologies, and next-generation organic electronics.

The conversion of triplet excitons to useful energy is fundamentally important for many advanced photonic and optoelectronic applications[1–3]. Understanding and controlling the behaviour of triplet excitons can lead to significant advancements in device efficiency and functionality, including more efficient OLEDs, improved solar cells, and novel applications in security and bioimaging[4–6]. In a typical luminophore, the key factors affecting triplet excitons include the process of intersystem crossing (ISC) from a singlet excited state to a triplet excited state and the deactivation processes via radiative (phosphorescence) and non-radiative transitions from a triplet excited state to the singlet ground state. The rate constant of non-radiative decay from the triplet excited state ($k_{nr}(T)$) is significantly influenced by factors such as temperature, the medium involved, and emitter concentration through energy transfer mechanisms[7–10]. The rate constants of ISC (k_{isc}) and radiative emission from triplets (k_p) are highly dependent on the structural and compositional characteristics of the chromophore and can be tuned from 10^{-2} to 10^6 s^{-1}.

One of the most established strategies for triplet harvesting involves the spin-mixing of singlet and triplet excited states[11]. Spin-orbital interactions induced by heavy metals such as iridium[12–14], copper[1,15], and platinum[16,17]; or heavy atoms such as bromine[18,19], iodine[20], and xenon[21], are quite effective at harvesting triplet excitons. However, these materials suffer from various challenges, such as stability issues, toxicity, scarcity, synthetic complexity, and high cost. Consequently, organic phosphorescent materials have garnered significant attention due to their facile synthesis, cost-effectiveness, tuneable emission, stability, and easy processability[22]. While it was generally observed that metal-free organic molecules exhibited phosphorescence emission only at cryogenic temperatures (77 K) in a rigid matrix[23], recent studies have demonstrated room-temperature phosphorescence (RTP) from various

[1]Department of Inorganic and Physical Chemistry, Indian Institute of Science, Bengaluru, Karnataka, India. [2]Department of Chemistry, Indian Institute of Science Education and Research, Tirupati, Andhra Pradesh, India. [3]Department of Chemical and Pharmaceutical Sciences, University of Trieste, Trieste, Italy. ✉e-mail: jatish@iisertirupati.ac.in; nhickey@units.it; thilagar@iisc.ac.in

classes of organic compounds, including aromatic carbonyl compounds[24], carbazole derivatives[25,26], phosphorus-containing compounds[27,28], conjugated polymers and oligomers[29] and hydrogen-bonded systems[30].

Recent times have seen a growing emphasis on organic persistent room temperature phosphorescent (pRTP) materials, which exhibit long-lasting emissions with lifetimes (τ) greater than 0.1 sec[31]. Among the commonly explored strategies for achieving prolonged organic afterglow, optimizing the incorporation of heavy elements[18] or modifying functional groups has been extensively studied, primarily to enhance intersystem crossing[32]. In other approaches, strong crystalline interactions, such as hydrogen bonding or halogen bonding, are utilized to stabilize the excited states[33–35]. In these materials, the rigid crystalline environment effectively suppresses non-radiative decay pathways by restricting molecular motions, thereby enhancing the phosphorescence efficiency[36]. Although these approaches are very propitious for developing metal-free organic phosphors, they still have limitations to practical applications because of the limited processability of crystalline materials. On the other hand, polymer-doped organic RTP materials offer several advantages due to their amorphous nature, improved processability, and thermal and chemical stability[37]. Additionally, achieving pRTP with improved efficiency (in terms of lifetime and quantum yield) from chromophores doped at very low weight percentages in polymer media by reducing the aggregation caused quenching opens an avenue for economically efficient emitters.

Poly(methyl methacrylate) (PMMA) is a well-known polymer for creating a rigid environment for small-molecule phosphors when these are embedded in the matrix by physical blending[37]. The interwoven structures and long polymer strands can ensure a rigid environment for the phosphor, with multiple interaction sites to facilitate efficient phosphorescence[29]. PMMA based thin films also have high transparency and chemical resistance, thereby enhancing the durability and longevity of the phosphorescent materials. However, ambient temperature can induce vibration and diffusion motions, such as β (side group conformation reorganization) and α (micro-Brownian motions of main-chain segments) transitions in an amorphous polymer matrix[38,39]. These transitions can lead to vibrational dissipation of triplet energy of phosphors, resulting in complete quenching of phosphorescence. Thus, improving and refining the structural designs and compositional factors of the phosphors to enhance the triplet emission continues to be a vital research domain in the field of phosphorescence research.

Recent decades have witnessed remarkable progress in exploiting BN/CC isosterism in material science and biology[40,41]. According to El-Sayed's rule, spin-orbit coupling between singlet and triplet states of different symmetry enhances intersystem crossing, leading to faster triplet population[42]. The inclusion of a BN moiety in an aromatic system can induce singlet/triplet excited states of different symmetry, such as charge transfer (CT, BN) and locally excited (LE, π−π*) states, thereby facilitating ISC. Hence, the integration of BN moieties into chromophores has proven to be advantageous in developing delayed emissive materials[43], which serve as efficient emitters in OLED applications[44,45]. Recently, our group reported that PMMA thin films dispersed with 1 wt% of naphthyl-containing aminoboranes exhibited persistent room temperature phosphorescence from the molecular state, with an average lifetime of approximately 0.5 sec and phosphorescence quantum yield of 2%[46]. In addition, we also investigated the circularly polarized luminescence (CPL) property of aminoboranes tagged with point chirality in the molecular system; however, these systems were ineffective in harvesting triplet excitons[47].

As stated above, rigidification of chromophores by crystallization/coordination with heavier elements/ polymer matrix enhances radiative $T_1 \rightarrow S_0$ transitions[18,29,34]. Thus, by structurally locking two aminoborane units via an atropisomeric axis, we targeted to suppress molecular motion-induced non-radiative decay, promote ISC through improved spin-orbit coupling, and impart chiroptical activity. Structures possessing axial chirality induced by steric inflexibility are capable of exhibiting persistent phosphorescence even at room temperature in addition to obvious chiroptical properties; however, such reports remain relatively scarce[48–50]. In this target, we systematically examined the pRTP properties of chirally locked aminoboranes (***R/S*-(BN)$_2$**) and compared them to their achiral mono-core counterpart **(BN)$_1$** and its non-borylated analogue **2-NaphNH$_2$** (Fig. 1). Our detailed mechanistic investigations and theoretical analyses demonstrate that single-molecular RTP is significantly enhanced upon borylation and further improved by introducing axial chirality, culminating in a phosphorescence quantum yield of 9.2% and a lifetime of 0.9 s at room temperature for 1 wt% ***R*-(BN)$_2$** dispersed in PMMA matrix. Furthermore, the axially chiral aminoboranes displayed CPL in dichloromethane solutions with a dissymmetry factor of ~10^{-3}. These phosphors, with intriguing afterglow properties, were successfully utilized in hidden writing applications, highlighting their broad potential for practical use.

Results

Synthesis and Characterization

The precursor compound, **2-NaphNH$_2$**, was synthesized by following a previously reported method[51]. The final compounds, **(BN)$_1$** and the optically pure axially chiral aminoboranes, ***R*-(BN)$_2$** and ***S*-(BN)$_2$**, were synthesized by modifying our previous methodology[46,47,52]. This involves the lithiation of arylamine with ^{n}BuLi at approximately −78 °C, followed by capturing the *N*-centred anion with dimesitylboron fluoride (Scheme S1). Each product was purified by multiple silica gel column chromatography to obtain analytically pure samples. The compounds were then characterized using NMR (^{1}H and ^{13}C) spectroscopy, high-resolution mass spectrometry, and high-performance liquid chromatography (with a chiral stationary phase for the chiral samples) (Figs. S1-S13).

Molecular Structures

Slow evaporation of dichloromethane/acetonitrile (1:1) solutions of ***R*-(BN)$_2$** and ***S*-(BN)$_2$** under ambient conditions produced single crystals

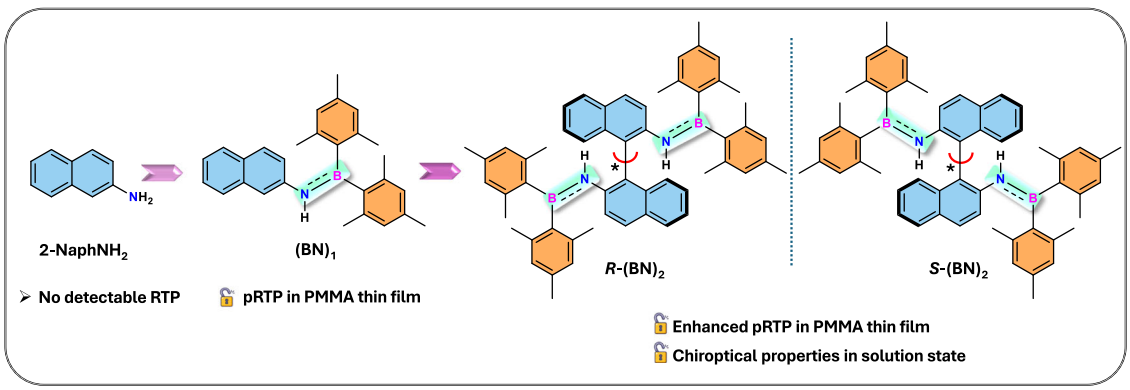

Fig. 1 | Representation of the molecular design strategy. The introduction of axial chirality for steric-hindrance-caused rigidification of the dual-core system to achieve enhanced pRTP properties and chiroptical properties.

suitable for X-ray diffraction studies. However, **(BN)$_1$** did not crystallize in any of the crystallization methods attempted. The crystallographic data and refinement parameters are listed in Table S1. Both crystals belong to the same Sohncke $P2_12_12$ space group with similar orthorhombic unit cell parameters. The asymmetric units of both crystals contain one **(BN)$_2$** molecule and co-crystallized disordered acetonitrile/dichloromethane molecules (Fig. 2a, b). The co-crystallized solvent molecules are superimposed and occupy an analogous crystal site, with refined partial occupancy factors of 0.281(6)/0.061(3) for ***R*-(BN)$_2$C** and 0.462(8)/0.124(3) for ***S*-(BN)$_2$C**, respectively [**C** indicates the solvent co-crystallized structure]. The refinements of the Flack parameters confirm the absolute configurations and demonstrate that ***R*-(BN)$_2$C** and ***S*-(BN)$_2$C** are enantiomeric crystals (Fig. S14).

The steric hindrance to rotation around the C1-C1' bond linking the two naphthalene units produces the canonical axial chirality in ***R*-(BN)$_2$** and ***S*-(BN)$_2$**. In the crystals, the two atropisomeric molecules assume a pseudo-dissymmetric conformation belonging to the C_2 symmetry point group, with the pseudo-twofold axis corresponding to a helical axis (Fig. 2c). In terms of helical chirality, the two atropisomers, ***R*-(BN)$_2$** and ***S*-(BN)$_2$**, display naphthalene groups oriented in anticlockwise (**M**, minus) and clockwise (**P**, plus) directions, respectively, resembling a left-handed and right-handed two-blade propeller when viewed along the pseudo-twofold axis perpendicular to the chiral axis (Fig. 2c). The torsion angles C2-C1-C1'-C2' are -106.1(1)° and 106.2(2)° for ***R*-(BN)$_2$(M)** and ***S*-(BN)$_2$(P)**, respectively, with dihedral angles between the mean planes of the two naphthalene groups being 73.71(2)° and 74.33(4)°.

Photophysical properties

The absorption and emission properties of the compounds were studied at 25 °C in dilute solutions (concentration = 10 μM) using solvents with varying dielectric constants, namely cyclohexane (Chex: ∈ (dielectric constant): 2.0), dichloromethane (DCM: ∈: 8.9), and acetonitrile (ACN: ∈: 37.5). The enantiomeric compounds exhibited comparable photophysical properties (Figs. 3a, b and S18c). Thus, ***R*-(BN)$_2$** is taken as a representative example to describe the optical properties.

Solutions of **(BN)$_1$** and ***R*-(BN)$_2$** showed strong absorption in 250−350 region whereas **2-NaphNH$_2$** displayed weaker absorption bands (Fig. 3a). The absorption spectra of **(BN)$_1$** and ***R*-(BN)$_2$** revealed negligible changes in terms of peak position with increasing the solvent polarity, indicating the nonpolar nature of the ground state in these molecules (Fig. S18b and S18c). The DFT-calculated ground state dipole moments for **(BN)$_1$** (μ_g = 0.88 Debye) and ***R*-(BN)$_2$** (1.12 Debye) are much smaller than that of **2-NaphNH$_2$** (2.30 Debye), which validates the nonpolar ground state in these compounds[46,53,54]. The absorption spectra of **2-NaphNH$_2$** showed slight shift for the lower energy absorption band at ~340 nm with increase in the solvent dielectrics (Fig. S18a). However, the band at ~260 nm with vibrational pattern did not show any significant solvent effects. Based on these observations and the theoretical interpretation, the absorption bands at ~260 nm and ~340 nm were assigned to π-π* and the n-π* transitions, respectively, which is consistent with the typical range of these transitions[55].

The simulated absorption spectra, obtained through time-dependent density functional theory (TD-DFT) calculations on the ground state optimized structure obtained by using CAM-B3LYP functional and 6-31 G(d,p,) basis set (Fig. S15), reveal intense absorption peaks at 220 nm, 299 nm (for **2-NaphNH$_2$**); 220 nm, 246 nm and 279 nm (for **(BN)$_1$**); 250 nm and 288 nm (for ***R*-(BN)$_2$**) (Fig. S16). The solvent effects in the TD-DFT calculations were modelled by the polarizable continuum model (PCM), using the integral equation formalism variant (IEFPCM)[56] which simulates the solvent as a continuous polarizable medium. This approach approximates the experimental environment by accounting for solute-solvent interactions, particularly dielectric polarization effects. These results closely align with the experimental plot, confirming the suitability of the selected computational methods (Fig. S16 & S17). The major vertical transitions and the respective molecular orbital contributions are summarised in Table S2. The band at 340 nm, which corresponds to the n-π* transition of the **2-NaphNH$_2$**, is faintly present in both **(BN)$_1$** and ***R*-(BN)$_2$**

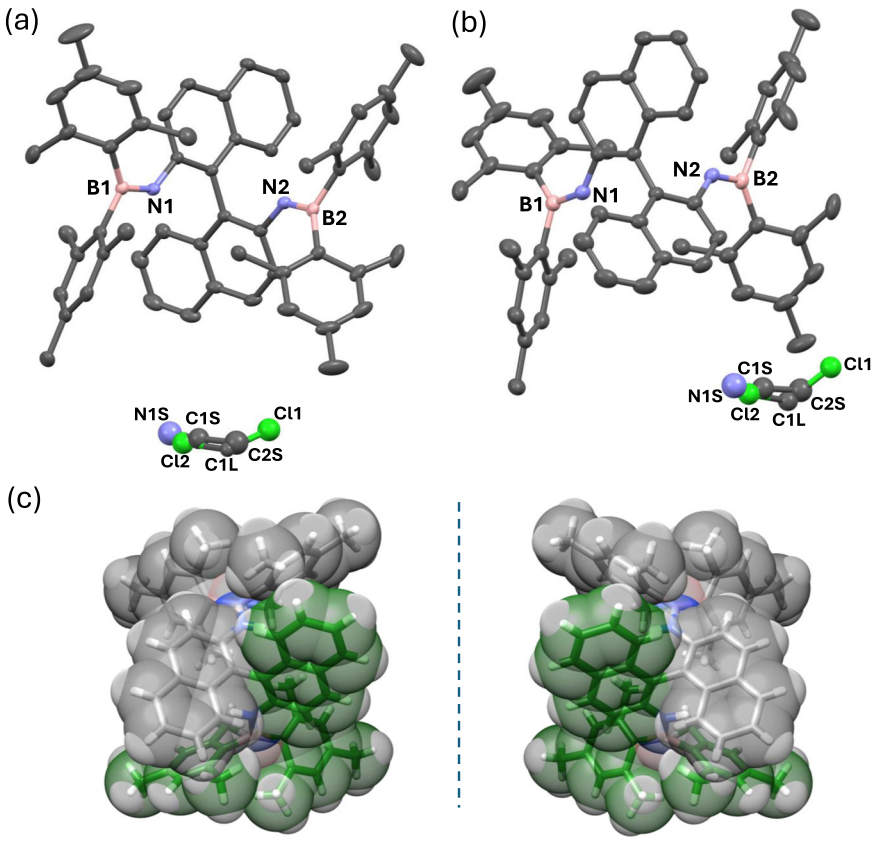

Fig. 2 | Crystal structures of the *R*/*S*-(BN)$_2$. Asymmetric units of (**a**) ***R*-(BN)$_2$C** and (**b**) ***S*-(BN)$_2$C** obtained from X-ray diffraction analysis (thermal ellipsoids are shown at the 50% probability level, H atoms are omitted for clarity). **c** The two enantiomeric dissymmetric molecules viewed along the pseudo twofold axis: ***R*-(BN)$_2$(M)** (left) and ***S*-(BN)$_2$(P)** (right) (The carbon atoms of the two halves of the molecules related by the pseudo-twofold axis are coloured in green and gray).

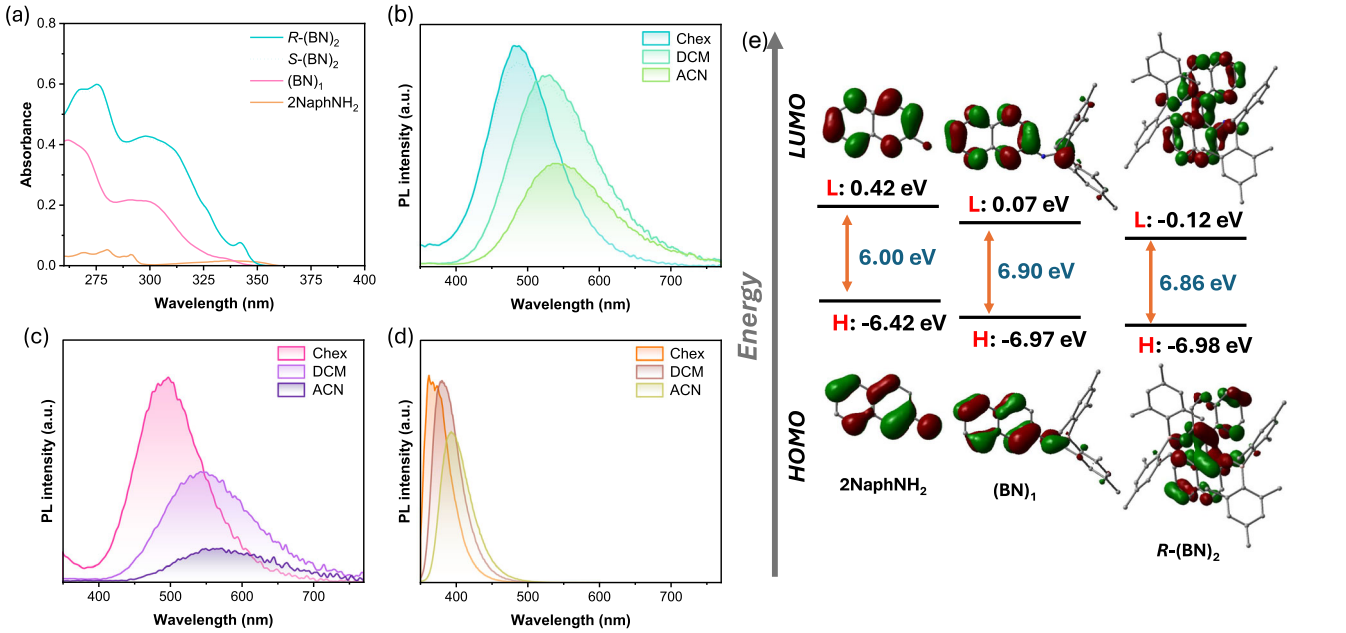

Fig. 3 | Optical properties and theoretical analysis of the compounds in solution phase. a UV-Vis absorption spectra of **2-NaphNH$_2$**, **(BN)$_1$**, ***R*-(BN)$_2$** (solid line) and ***S*-(BN)$_2$** (dotted line) in cyclohexane solution ($c = 10$ μM). PL spectra of (**b**) ***R*-(BN)$_2$** (solid line); ***S*-(BN)$_2$** (dotted line), **c** **(BN)$_1$**, and (**d**) **2-NaphNH$_2$** in solvents of varying dielectrics ($c = 10$ μM), **e** Frontier molecular orbitals (iso value = 0.04) generated from the ground state [S_0] geometries using the CAM-B3LYP/6-31 G(d,p) level of theory [with IEFPCM model for cyclohexane].

along with the π-π* transition band (Fig. 3a). The incorporation of the BN entity has significantly enhanced the molar absorptivity of the compounds (Table S3); this observation is similar to other previous studies[57]. The molar extinction coefficient of ***R*-(BN)$_2$** is about 1.5 times greater than the value observed for **(BN)$_1$** in the cyclohexane solution, likely due to the increased number of chromophores in ***R*-(BN)$_2$** (Table S3). Compared to **(BN)$_1$**, the absorption spectra of ***R*-(BN)$_2$** showed a red shift in all solvents, likely due to the extended π-conjugation in the binaphthyl moiety. This behaviour is similar to that observed in isolated chromophores and their corresponding binaphthyl derivatives previously reported elsewhere[58].

Further, to understand the nature of the molecular orbitals involved in the electronic transitions, the frontier molecular orbitals (HOMO and LUMO), energy levels, gaps, and electronic density distributions were analysed. The DFT results revealed that for all the molecules the HOMO comprised the charge distribution on the naphthyl fragment with significant contribution from the *C*-2 substituted amine *N* atom, while the charge density on the LUMO is mainly localized on the naphthyl or binaphthyl core and Boron atoms with no contribution from the amine *N* atom (Fig. 3e). This is an indication that vertical transition is of a locally-excited (LE) dominated character. In the case of **(BN)$_1$**, both the HOMO and LUMO levels are more stabilized compared to those of **2-NaphNH$_2$**, as expected due to the substitution by the electron-deficient dimesityl boron entity. The relatively reduced HOMO–LUMO gap in **2-NaphNH$_2$** is reflected in its absorption, which occurs in the longer wavelength range (Table S3)

The emissions of **2-NaphNH$_2$** solutions in solvents of increasing dielectrics showed a small bathochromic shift of 28 nm ($\lambda_{em} = 394$ nm in acetonitrile and 366 nm in cyclohexane) in comparison to those observed for **(BN)$_1$** and ***R*-(BN)$_2$** (Fig. 3b–d and Table S3). Both **(BN)$_1$** and ***R*-(BN)$_2$** showed a high positive solvatochromic shift of the emission maxima with a decreased emission intensity in high polar solvent like acetonitrile. This behaviour is typically observed in the aminoborane systems, indicative of the highly polar (+B=N-) nature of the excited state. A pronounced spectral shift is a characteristic of an emission that originate from the charge-transfer (CT) state. Both **(BN)$_1$** and ***R*-(BN)$_2$** displayed highest stokes shift in polar acetonitrile solvent (20918 cm^{-1} for **(BN)$_1$** and 18146 cm^{-1} for ***R*-(BN)$_2$**), further confirming that the emissive state is a polar CT state (Table S3). The excitation spectra of the samples, obtained for the corresponding emission maxima are spectrally identical to the respective absorption spectra, indicating that these emissions originate from the initially excited single molecular species (Fig. S19). These results suggest that the emissive state in **2-NaphNH$_2$** is a n-π* state with major LE nature and both **(BN)$_1$** and ***R*-(BN)$_2$** have a polar charge-transfer state as a result of BN inclusion.

Time-correlated single photon counting (TCSPC) measurements were performed on all compounds in different solvents to gain further insight into the excited state of these compounds. Compounds displayed lifetime values (τ) in the nano second range consistent with the fluorescent nature of the emissions (Table S4). Photoluminescence quantum yields (Φ_{PL}) were measured in different solvents by a relative method[59]. All the compounds were found to be weakly emissive in the solution state (Φ_{PL} of upto ~17%), similar to our previous observations on aminoboranes (Table S4)[46,47]. Higher dielectric solvents promoted the non-radiative channels form the CT excited state which resulted a notable decrease in the Φ_{PL} value in polar solvents.

The pristine solids of **2-NaphNH$_2$**, **(BN)$_1$** and ***R*/*S*-(BN)$_2$** showed emission maxima at 395 nm, 465 nm and 370 nm upon excitation at 300 nm respectively (Fig. S20a). The absolute Φ_{PL} of the pristine solid samples were found to be 43.1% for ***R*-(BN)$_2$**, 39.5% for ***S*-(BN)$_2$**, and 32.1% for **(BN)$_1$** (Table S5). The variation in Φ_{PL} in the solid state among the enantiomers of compound **(BN)$_2$** is similar to our previous results, suggesting that the arrangement of ***R*-(BN)$_2$** and ***S*-(BN)$_2$** in the solid state may slightly differ, leading to discrete photoluminescence features. Several other reports also indicate that enantiomers can display notably different photoluminescence quantum yields in the solid state[60,61]. We also examined the phosphorescence emission properties of these compounds in the solid state. The solid samples of these compounds did not show any significant phosphorescence at room temperature (RT) even in the absence of air, indicating that interactions or the geometrical restrictions in the solid or crystalline state are not conducive to triplet exciton harvesting (Figs. S20b–d).

Molecular persistent room-temperature phosphorescence properties

The emission properties of PMMA-based thin films with varying doping concentrations (1, 3, 6, 10, 25 and 50 wt %) of samples were investigated to determine the optimal doping concentration and analyse the effect of

concentration-induced quenching in phosphorescence (Fig. 4, S21 and Table S6). The time-gated emission spectra of thin films revealed that ***R/S*-$(BN)_2$** samples displayed an enhanced phosphorescence emission compared to the **$(BN)_1$**, whereas **2-NaphNH_2** did not show any detectable signals (Fig. S22). Notably, fluorescence spectra of PMMA films of aminoboranes exhibited distinct LE and CT bands at 365 nm and ~430 nm, respectively (Fig. 4a and S21a). To further validate the attribution of these bands, we conducted emission studies in media of varying viscosity. High-viscosity solvents are known to retard the molecular motions, making the LE emission bands more observable. In hexane (viscosity (η) = 0.296 centipoise), we detected a small peak at 330 nm and a broad band at 484 nm (Fig. 5b). The PL band at the red end of the spectrum corresponds to the CT band observed in cyclohexane solution ($\lambda_{em\ [Chex]}$ = 485 nm). When the viscosity was increased by mixing hexane with a more viscous solvent like paraffin (η = 62.6 centipoise) (hexane/paraffin 1:1), the high-energy band became more prominent, revealing vibrational patterns. Furthermore, the emission spectra recorded in paraffin solvent exhibited a higher relative intensity of the LE band compared to the CT band. The increased viscosity of the media restricted the fast structural reorganization in the excited state, thereby stabilizing the otherwise less stable LE band along with the CT band. In short, the dual emission characteristics of the compounds in viscous media are comparable to the emission characteristics in the PMMA matrix, confirming the LE and CT nature of the spectrum.

As the doping concentration is increased in the PMMA matrix, the fluorescence spectra displayed significant variation in the intensity ratio of LE and CT contributions. At higher doping levels, an increase in the CT contribution was observed for both the ***R/S*-$(BN)_2$** and **$(BN)_1$** sample. The rigid geometry of ***R/S*-$(BN)_2$** resulted in a consistently higher LE contribution compared to **$(BN)_1$** across all doping levels. Elevated doping concentrations in the PMMA matrix limit the phosphor-polymer interactions, thereby increasing detrimental intermolecular interactions between the phosphors. These interactions might have favoured the adoption of a CT geometry over an LE geometry.

Among the examined thin films, the optimum phosphor doping concentration was found to be 1 wt% for ***R/S*-$(BN)_2$** and **$(BN)_1$** in the PMMA matrix, as shown in Fig. 4c–h. At higher phosphor concentrations,

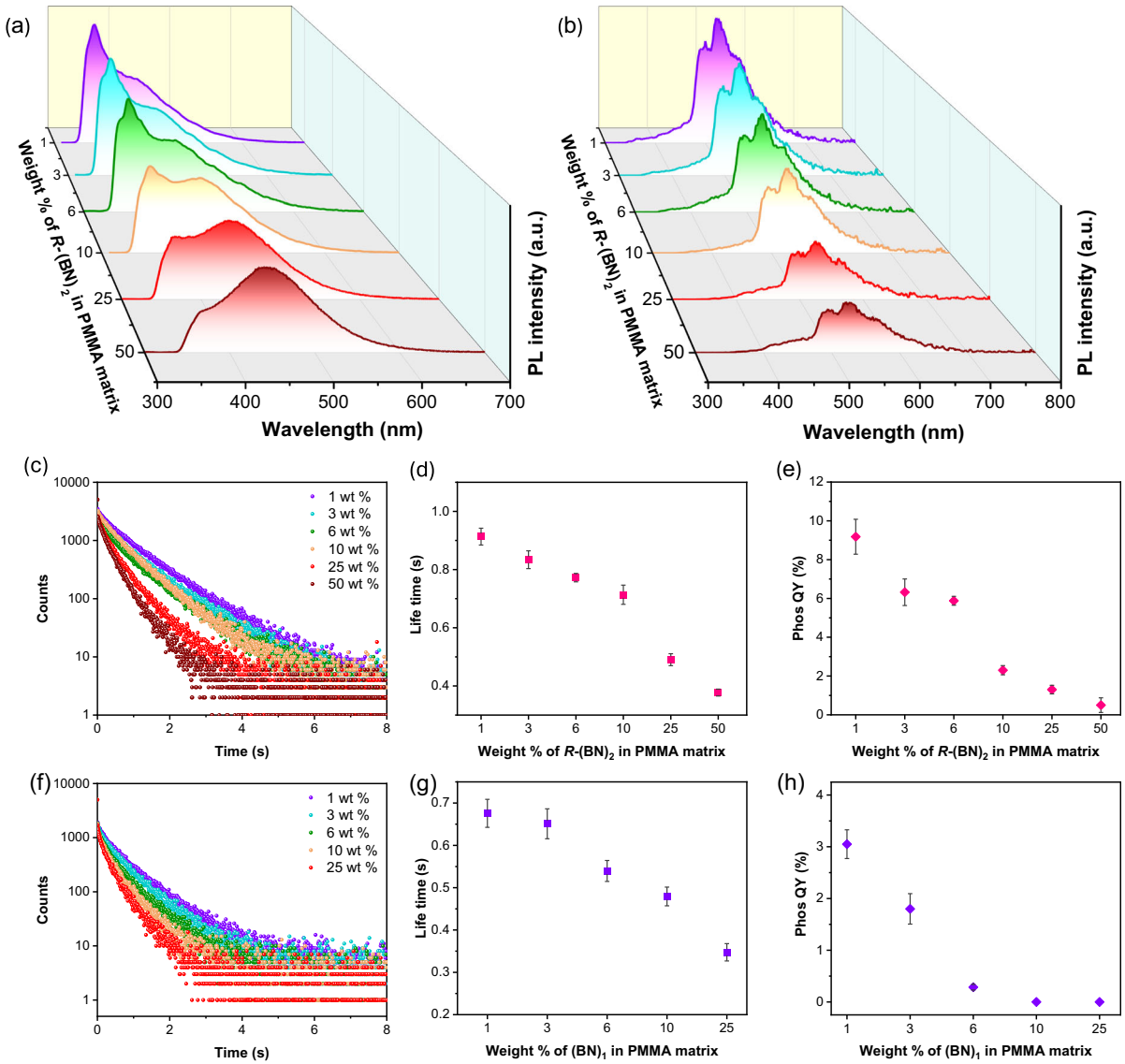

Fig. 4 | Optical properties of PMMA thin films with different phosphor concentrations. a PL spectra and (**b**) delayed PL spectra of ***R*-$(BN)_2$** at varying phosphor concentrations. **c**, **f** Time-resolved decay profiles of ***R*-$(BN)_2$** and **$(BN)_1$** monitored at 530 nm and 525 nm, respectively. **d**, **g** Phosphorescence lifetimes, and (**e**, **h**) phosphorescence quantum yields of ***R*-$(BN)_2$** and **$(BN)_1$** at different concentrations in PMMA. All the measurements taken under vacuum at 298 K (Delay = 50 μs, λ_{ex} = 280 nm) (Error bars represent standard deviation from three independent measurements (n = 3); The x-axis is not to scale and has been adjusted for better visualization in panels (**d**, **e**, **g**, **h**)).

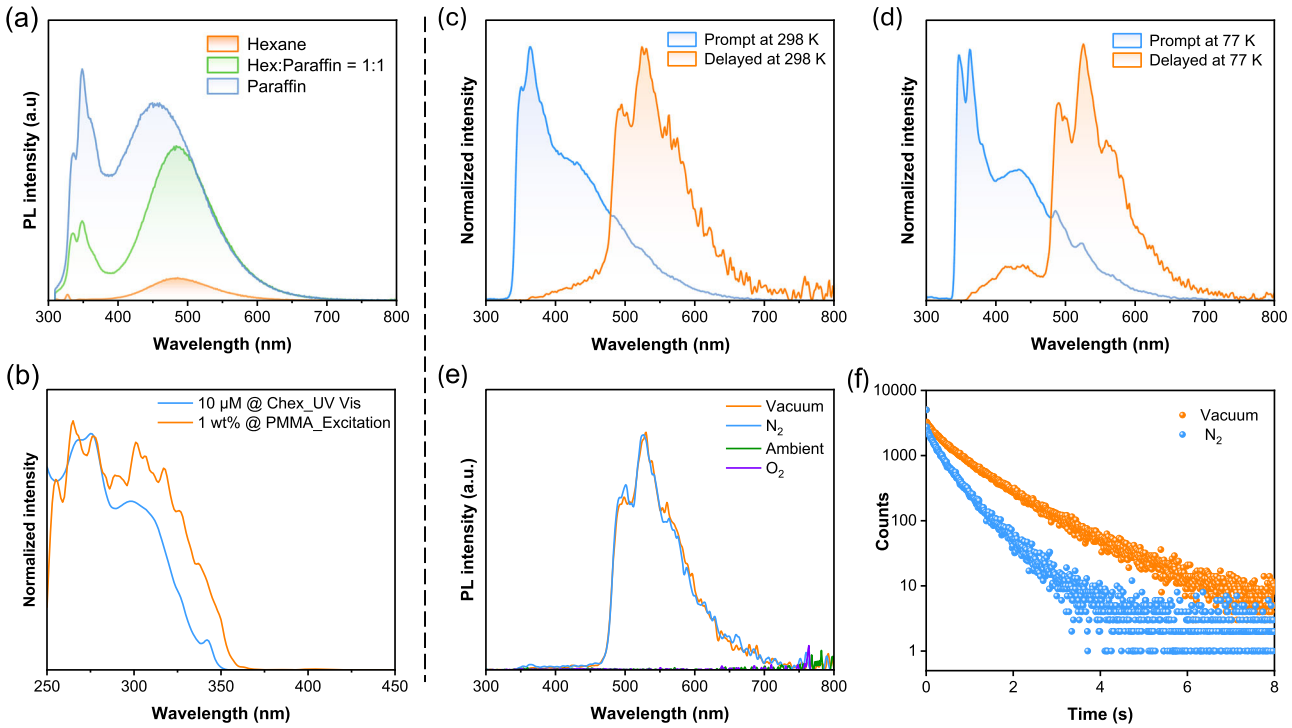

Fig. 5 | Molecular optical properties of *R*-$(BN)_2$ in viscous and rigid media. **a** Fluorescence spectra in hexane, paraffin, and a hexane/paraffin mixture (1:1) (concentration = 10 μM). **b** Absorbance spectrum (in cyclohexane solution) and excitation spectrum (1 wt% in PMMA), monitored at λ_{em} = 530 nm. Prompt and delayed emission spectra (1 wt% in PMMA matrix) under vacuum conditions (**c**) at 298 K and (**d**) at 77 K. **e** Delayed emission spectra (1 wt% in PMMA matrix) under different environments. **f** Time-resolved decay kinetic profiles measured at 530 nm under vacuum and N_2 atmospheres (delay = 50 μs, λ_{ex} = 280 nm).

self-quenching is likely responsible for the observed reduction in phosphorescence quantum yield, with a complete disappearance of the phosphorescence band in the neat film (100 wt%) for ***R*/*S*-$(BN)_2$** and 50 wt % for **$(BN)_1$** (Table S6). We also analysed the phosphorescence lifetime for various concentrations of phosphors dispersed into PMMA. A significant decrease in the average lifetime was observed as the phosphor concentration exceeded 10 wt %, attributed to dominant non-radiative self-quenching pathways at higher concentrations. These observations are consistent with the enhanced fluorescence quantum yield (~70.3% for ***R*-$(BN)_2$**, 65.6% for ***S*-$(BN)_2$** and 44.8% for **$(BN)_1$**) at the 1 wt % dispersed PMMA film, compared to the neat film samples (~45.5% for ***R*-$(BN)_2$**, 40.3% for ***S*-$(BN)_2$** and 35.6% for **$(BN)_1$**). This suggests that intermolecular interactions are detrimentally impacting both the phosphorescence and fluorescence efficiencies. The restriction of molecular motion-mediated non-radiative channels in the rigid polymer matrix and suppressed intermolecular interactions of the molecule at a low doping concentration effectively facilitated the phosphorescence of triplet excitons even at room temperature. Additionally, the enhanced phosphorescence quantum yield of the thin film at 1 wt% concentration, and the spectrally identical excitation spectra of phosphorescence band (530 nm) to that of molecularly dispersed solution state absorption spectrum clearly indicates that the emission is originating from monomeric species rather than from aggregates (Fig. 5c).

Intriguingly, the time-gated spectra of PMMA thin films embedded with 1 wt% ***R*-$(BN)_2$** showed a weak band at ~ 430 nm in addition to the phosphorescence band at 530 nm (Fig. 5a). This band maxima matched well with the ^{1}CT fluorescence which indicated the possibility of delayed fluorescence (DF) (Table S7). The films exhibited clear vibrational progression at 77 K compared to 298 K, likely due to the reduced thermal motion of the molecules at the lower temperature, which allows the vibrational structure to be more distinctly resolved. In contrast, at the higher temperature of 298 K, the increased thermal motion broadens these features, making them less distinct (Fig. 5a). Furthermore, the emission features of the samples were examined under ambient, N_2, and O_2 conditions. Under ambient and O_2 conditions, the delayed PL band completely disappears and is restored when the sample is placed under vacuum. Although the emission intensity was unaffected for the 530 nm band, there was a reduction in average lifetime of the emitter under an N_2 atmosphere (τ = 510 ms) compared to vacuum conditions (τ =930 ms) (Fig. 5e, Table S8). These observed variations in the phosphorescence features could be due to the trace amount of O_2 impurities in the N_2 (Fig. 5d). The pronounced susceptibility of the delayed PL bands to oxygen further supports the involvement of the triplet excited state in the radiative processes of these compounds. Other important phosphorescence parameters, including the quantum yield and decay rate constants for the 1 wt% dispersed PMMA thin films are summarized in Table S9.

The synergistic effect of borylation and the introduction of the atrop axis significantly enhances the pRTP features of ***R*/*S*-$(BN)_2$**, as evidenced by their phosphorescence quantum yield values (9.2% for ***R*-$(BN)_2$**; 8.7% for ***S*-$(BN)_2$** compared to the **$(BN)_1$** with Φ_P = 3.0% and **2-NaphNH$_2$** with non-detectable phosphorescence). Similarly, the average phosphorescence lifetime values of these samples indicate that the chiral ***R*/*S*-$(BN)_2$** have an enhanced lifetime compared to **$(BN)_1$** (Table S10). This enhancement in pRTP properties for the dual core ***R*/*S*-$(BN)_2$** molecules compared to the mono-core **$(BN)_1$** could be attributed to the steric-induced rigidification caused by the introduction of the atrop axis in the aminoboranes, which resists the molecular motions at room temperature. This is also evident from the fluorescence spectra of 1 wt% dispersed thin films of **$(BN)_1$** and ***R*/*S*-$(BN)_2$** (Fig. S23). The LE band is more prominent in ***R*-$(BN)_2$** compared to **$(BN)_1$**, indicating reduced molecular motions. Additionally, **$(BN)_1$** shows a broader full width at half maximum (FWHM), while ***R*-$(BN)_2$** displays a much sharper band, reinforcing the steric-caused hindrance to molecular motions. Together with enhanced spin-orbit coupling achieved in the chiral system (Table S10), these factors contribute to the superior pRTP performance of the chirally locked aminoboranes.

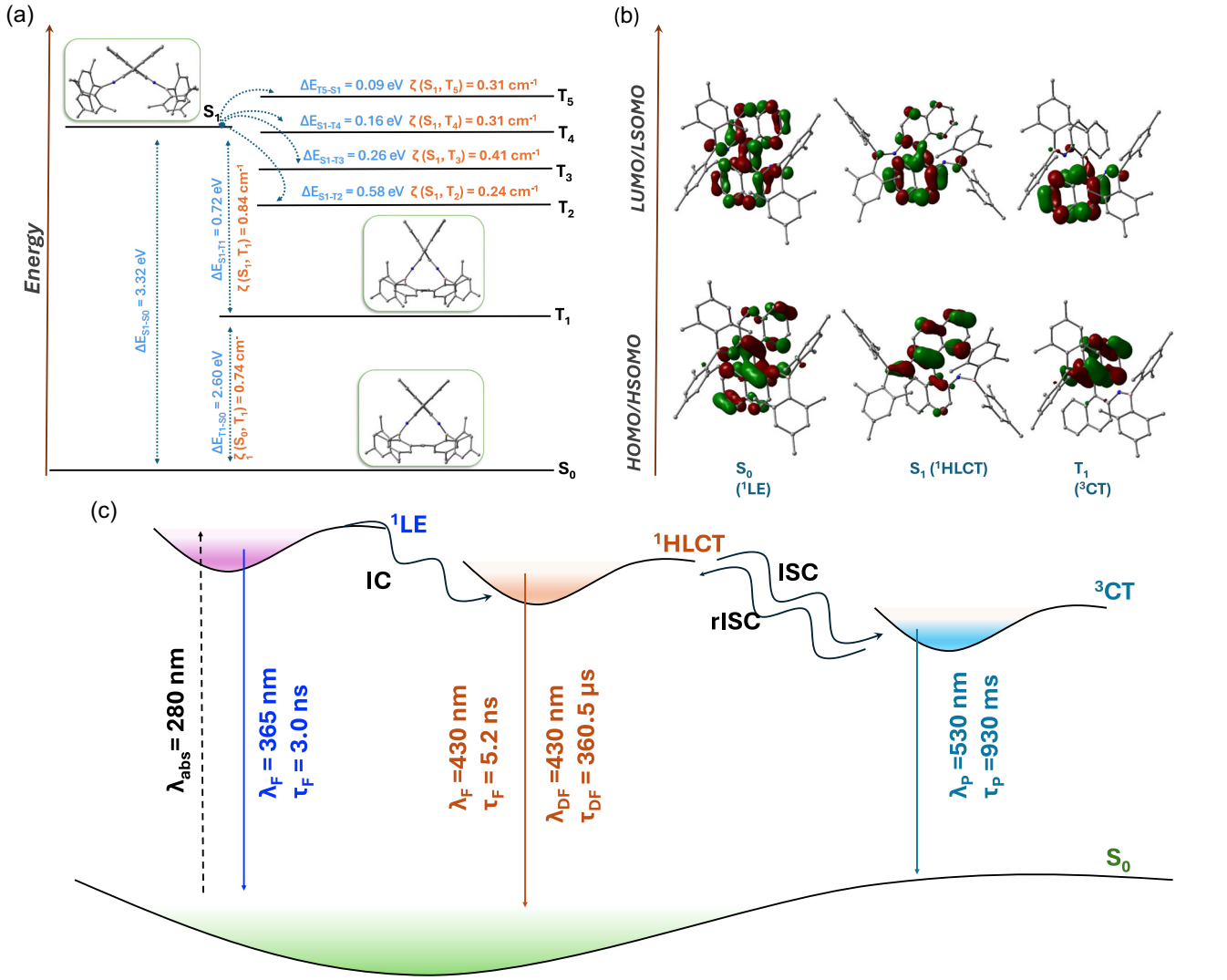

Fig. 6 | Theoretical analysis of the phosphorescence process. a Schematic representation of the TD-DFT calculated energy gaps of ***R*-(BN)$_2$**; optimised geometries of S_0, S_1, T_1 and calculated SOC constant values. **b** Frontier molecular orbitals of ***R*-(BN)$_2$** in S_0, S_1 and T_1 state obtained from DFT and TD-DFT calculations using Gaussian 16 software with B3LYP functional and 631G-(d,p) basis set (|isovalue|= 0.04). **c** Potential energy diagram depicting one of the plausible photophysical pathways occurring at 298 K in the 1 wt % ***R*-(BN)$_2$** dispersed in PMMA matrix. [F Fluorescence, DF Delayed fluorescence, P Phosphorescence].

Theoretical studies

Detailed theoretical calculations were performed to compare and analyse the different triplet emission behaviours and to understand the underlying mechanism for the pRTP process involved in these compounds. The geometry of the first singlet and first triplet excited states (S_1 and T_1) were optimized by using standard computational methods (B3LYP functional/6-31 G(d,p) basis set). The frontier molecular orbitals of these excited states were analysed in detail to gain insights into their nature and to assess the feasibility of transitions between them. For **(BN)$_1$**, the analysis of frontier molecular orbitals (FMO) clearly states that the S_0 state is of LE character, whereas the S_1 state is of CT character (Fig. S24, Supplementary note 1). In the case of T_1, the naphthyl group and the BN entity show contributions in both HSOMO and LSOMO, making the state a hybridized local and charge-transfer (HLCT) excited state. In contrast, for ***R*-(BN)$_2$**, FMO analysis reveals that the S_0 state is also of LE character, but the S_1 state displays an HLCT character, where both naphthyl groups contribute to HSOMO and LSOMO. The T_1 state of ***R*-(BN)$_2$** is characterised by CT nature (Fig. 6b). According to El-Sayed's rule, different symmetries between the excited singlet and triplet states result in effective spin orbit coupling (SOC), leading to efficient ISC/rISC[42]. The SOC constant calculations were performed by considering 10 excited states in **(BN)$_1$** and ***R*-(BN)$_2$**, which provided the energy levels as well as the coupling constants between different singlet and triplet electronic states (Fig. 6a). The SOC calculated between S_1/T_1 and S_0/T_1 was found to be higher in the case of ***R*-(BN)$_2$** (ζ (S_1, T_1) = 0.84 cm^{-1} and ζ (S_0, T_1) = 0.74 cm^{-1}) compared to **(BN)$_1$** (ζ (S_1, T_1) = 0.26 cm^{-1} and ζ (S_0, T_1) = 0.21 cm^{-1}). This differences also accounts for the superior pRTP properties ***R*-(BN)$_2$** compared to **(BN)$_1$**.

Based on these results, the underlying processes and the electronic transitions involved in the single molecular pRTP of ***R*-(BN)$_2$** (1 wt% dispersed in PMMA) can be summarized in the following way. Upon photoexcitation at 280 nm, the molecule emits from the Franck−Condon state (^{1}LE) at 365 nm (τ = 3.0 ns). Additionally, some molecules emit from the ^{1}HLCT state at 430 nm (τ = 5.2 ns), leading to the dual-band fluorescence spectrum of the thin film. From the singlet state, the molecules undergo intersystem crossing to reach the triplet state (T_n). From the T_n state, molecules can revert to the ^{1}CT state via reverse intersystem crossing, resulting in delayed fluorescence at ~430 nm (τ = 360.5 μs). Furthermore, the molecules can radiatively decay from the T_1 (^{3}CT) state, giving rise to phosphorescence at ~530 nm (τ = 0.93 s) (Fig. 6c).

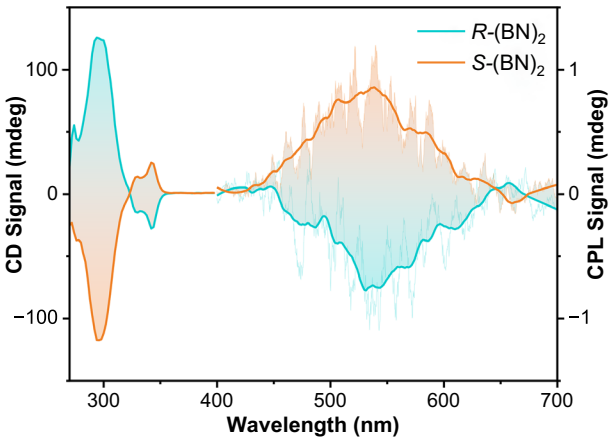

Fig. 7 | Chiroptical properties of aminoboranes. CD spectra (left) and CPL spectra (right) of ***R*-(BN)$_2$** and ***S*-(BN)$_2$** in dichloromethane solution (c = 0.5 mM, λ_{ex} = 300 nm) [CPL spectra were smoothed using the Savitzky-Golay filter method to enhance clarity].

Chiroptical properties

As the synthesized axially chiral compounds exhibited intriguing emission properties, we proceeded to analyse their chiroptical features. Materials with multitudinous inherent advantages have huge potential for sophisticated optical materials and devices. Recent times have witnessed an increased interest towards the development of CPL materials due to their importance in diverse applications such as 3D displays, optical data storage, and biological probes.

The ground-state chirality of the ***R*/*S*-(BN)$_2$** compounds were analyzed using circular dichroism (CD). The CD spectra of ***R*/*S*-(BN)$_2$** in dichloromethane solution (c = 0.5 mM) displayed mirror-imaged bands with a cotton effect in the 280–350 nm spectral range (Fig. 7). ***R*-(BN)$_2$** exhibited negative and positive bands at ~340 nm and ~300 nm, respectively, and vice-versa for ***S*-(BN)$_2$**. We further analyzed the correlation with computed rotatory strengths for ***R*/*S*-(BN)$_2$**, which supported their absolute configurations (Table S11). In the calculated electronic circular dichroism (ECD) spectra, ***R*-(BN)$_2$** displayed a negative Cotton effect (CE) at higher wavelengths, whereas ***S*-(BN)$_2$** exhibited a positive CE, consistent with experimental data. The absorption dissymmetry factors ($g_{abs} = (\varepsilon_L - \varepsilon_R)/(\varepsilon_L + \varepsilon_R)$; where ε_L and ε_R represent the molar extinction coefficient of left- and right-handed CPL respectively) were calculated from the experimental CD and absorption spectra, which lies in the range of $\pm 1.6 \times 10^{-3}$ (at ~340 nm) and $\pm 1.9 \times 10^{-3}$ (at ~295 nm), reflecting the intrinsic chiral nature of the molecule. The circularly polarized luminescence spectra of ***R*/*S*-(BN)$_2$** were measured in dichloromethane solution (c = 0.5 mM), showing CPL signals of opposite signs with $|\ g_{lum}\ |$ values of ~1×10^{-3}. The dissymmetry factor, g_{lum}, is defined as $2(I_L - I_R)/(I_L + I_R)$, where I_L and I_R represent the intensities of left- and right-handed CPL, respectively. These values fall within the typical range observed for small chiral organic molecules and indicate that the chirality is retained in the excited state as well. The sign of CPL signals matches with that of the CD at highest wavelength indicating that the similar chiral features of the molecules influence both the ground state (observed by CD) and the excited state (observed by CPL) chirality. Unfortunately, CPL signals were not observed in 1 wt% PMMA thin films. This absence can be attributed to several factors, including the lower doping concentration and the inhomogeneous alignment of the binaphthyl unit within the solid matrices. Unlike in solution, where molecules can freely rotate and achieve a uniform orientation, solid-state interactions can disrupt this alignment, which can be critical for generating detectable chiroptical signals (Fig. S25).

Demonstration of Security Writing Using pRTP Materials

We also attempted to visually observe the pRTP signals from the 1 wt% PMMA thin films of **(BN)$_1$** and ***R*/*S*-(BN)$_2$** under N_2 atmosphere by exciting them with UV irradiation, aiming to unveil the potential of these materials for anticounterfeiting applications. Both samples exhibited blue fluorescence (CIE coordinates of (0.18, 0.18) for **(BN)$_1$** ; (0.18, 0.16) for ***R*-(BN)$_2$**) and green phosphorescence (CIE coordinates of (0.27, 0.48) for **(BN)$_1$**, (0.32, 0.56) for ***R*-(BN)$_2$**) (Fig. 8d). Notably, the prolonged green afterglow of the ***R*/*S*-(BN)$_2$** samples lasted up to 3.2 s, whereas **(BN)$_1$** exhibited a shorter afterglow duration of 0.8 sec with lower intensity after the excitation ceased (Figs. 8a, b, S26). This distinct difference in emission behaviour inspired us to explore the security writing application. Using 1 wt% ***R*-(BN)$_2$** and **(BN)$_1$** doped PMMA inks, we created the digits '1180' in a digital font. Under UV illumination, all digits displayed bright blue fluorescence (Fig. 8c). Upon turning off the UV light, after 1 s, the hidden message "IISC" became visible, highlighting the potential of these materials in anti-counterfeiting applications.

Discussion

In this study, we explored an axial chirality-induced rigidification strategy to achieve enhanced pRTP properties and CPL in heavy-element-free compounds at the molecular level. A systematic analysis of the monocore and chiral dual-core systems allowed us to fine-tune the pRTP properties. The introduction of axial chirality and the incorporation of a BN moiety result in structural rigidity, effectively restricting molecular motions—such as vibrations and rotations—thereby reducing non-radiative decay and stabilizing the triplet state. This steric-hindrance-assisted design led to significant improvements in phosphorescence quantum yield and lifetime, with ***R*-(BN)$_2$** achieving a Φ_P of 9.2% (**S-(BN)$_2$** : 8.7%) and a lifetime of 0.9 s, substantially outperforming its monomeric counterpart **(BN)$_1$** (Φ_P = 3.0%, lifetime = 0.6 s).

The enhanced pRTP properties observed in chirally locked aminoboranes can be attributed to the synergistic effects of axial chirality and BN-enhanced spin-orbit coupling. These factors facilitate efficient intersystem crossing (ISC) via ^{1}HLCT and ^{3}CT transitions, followed by radiative decay in accordance with El-Sayed's rule. Notably, these improvements are achieved without relying on intermolecular interactions, highlighting the versatility of our design strategy. Moreover, this novel chiral chromophore also exhibited intriguing circularly polarized luminescence properties, further augmenting its utility.

Compared to other conventional approaches that depend extensively on intermolecular interactions to stabilize excited states or the inclusion of heavy elements to facilitate ISC, our steric-hindrance-based strategy in aminoboranes offers a unique advantage. The combination of structural rigidity and enhanced spin-orbit coupling through BN inclusion achieves superior performance within a single molecular framework. Beyond their fundamental significance, these non-toxic and cost-effective materials can be particularly important for high-resolution bioimaging, as they enable time-gated imaging independent of autofluorescence and excitation light scattering, as well as for organic scintillation for gamma-ray detection. The bright and prolonged afterglow observed in these samples were utilized in demonstrating anti-counterfeiting applications, further highlighting their potential in multilevel security applications, especially when combined with their chiroptical properties.

Methods

Materials and instruments

The chemicals were purchased from commercial suppliers and used as received. The target compounds were purified by multiple silica-gel column chromatography, followed by recrystallization and vacuum drying before experiments. ^{1}H and ^{13}C NMR spectra were recorded at 25 °C on a Bruker Avance 400 MHz NMR Spectrometer. High-resolution mass spectra were recorded on an Agilent 6545 Q-ToF spectrometer and Micromass Q-ToF High-Resolution Mass Spectrometer in standard spectroscopic grade solvents by the electrospray ionization method. Chiral HPLC analysis was performed on LC-20A Shimadzu HPLC System with a UV detector. Single-crystal X-ray data were collected at the Macromolecular Crystallography XRD1 beamline of the Elettra synchrotron (Trieste, Italy), employing the

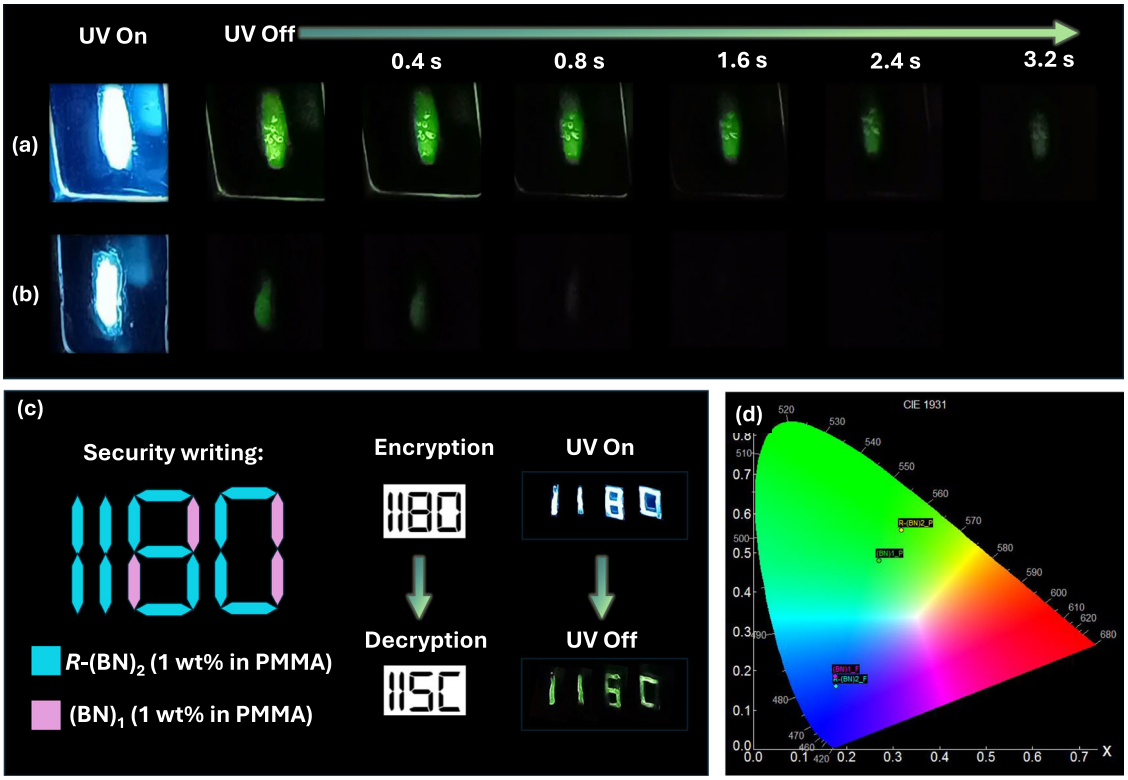

Fig. 8 | Demonstration of the security writing application. Luminescence photographs of pRTP samples with UV-340 nm irradiation and after removal of irradiation (**a**) 1 wt% ***R*-(BN)$_2$** in PMMA (**b**) 1 wt% **(BN)$_1$** in PMMA; **c** Demonstration of security writing using ink formulated from 1 wt% ***R*-(BN)$_2$** or **(BN)$_1$** in PMMA. (Background reflections under UV illumination were removed to enhance clarity) (**d**) Chromaticity diagram for 1 wt % in PMMA doped films of ***R*-(BN)$_2$** and **(BN)$_1$**.The samples are showing identical fluorescence, yet the chiral framework induced brighter phosphorescence and prolonged afterglow at 298 K in N_2 atmosphere.

rotating-crystal method with a Dectris Pilatus 2 M area detector. Absorption spectra and fluorescence emission spectra were recorded on a Shimadzu UV-2600 and Edinburgh Instruments FLS 980 spectrometers, respectively. The fluorescence quantum yield was measured using a Horiba Jobin Yuvon Fluoromax-4 spectrometer equipped with a Horiba Quanta-phi integrating sphere setup. Temperature-dependent (77 and 298 K) measurements were performed using an Oxford Instruments OPTISTAT DN2 cryostat controlled by an Oxford Instruments Mercury iTC temperature controller connected to the FLS 980 spectrometer. Time-gated emission spectra and decay profiles were recorded using a pulsed microsecond flash lamp (μF1) as an excitation source. CD and CPL spectra were recorded on JASCO J-810 CD spectropolarimeter and CPL-300 spectrofluoropolarimeter at room temperature.

PMMA Thin Film Preparation

PMMA and phosphors were individually dissolved in dichloromethane and sonicated thoroughly to obtain homogeneous solutions. The desired concentrations were prepared by mixing these solutions at the required ratios. PMMA thin films were then fabricated using the solution spin-coating method on a quartz substrate. The resulting films were allowed to dry at room temperature and were subsequently blow-dried using a cold-air blower for 10 minutes to ensure complete solvent removal.

Theoretical calculation

Density functional theory (DFT) and Time-Dependent DFT (TD-DFT) calculations were performed using the CAM-B3LYP functional with a 6-31 G (d, p) basis set, as implemented in the *Gaussian 16* package. The solvent effects in the TD-DFT calculations were modelled by the polarizable continuum model (PCM),) using the integral equation formalism variant (IEFPCM). Calculations were carried out in the gas phase for comparing the single molecular species characteristics in the PMMA matrix with 1 wt % doping concentration, as this concentration was expected to reflect conditions with no intermolecular interactions. The spin-orbit coupling matrix elements were calculated using the ORCA 5.2 programme.

Detailed information on materials and methods is provided in the Supplementary Methods section of the Supplementary Information file.

Data availability

All data generated or analysed during this study are included in this article (and its Supplementary Information files). The X-ray crystallographic coordinates for structures reported in this Article have been deposited at the Cambridge Crystallographic Data Centre (CCDC), under deposition number CCDC 2279763 for ***R*-(BN)$_2$C** [Supplementary Data 1], CCDC 2279764 for ***S*-(BN)$_2$C** [Supplementary Data 2]. These data can be obtained free of charge from The Cambridge Crystallographic Data Centre via www.ccdc.cam.ac.uk/data_request/cif. The numerical source data underlying the graphs and charts are given in Supplementary Data 3. The Cartesian coordinates of all optimized computational structures (ground electronic states) are provided in Supplementary Data 4. NMR spectra are provided in Supplementary Data 5.

Received: 27 September 2024; Accepted: 9 April 2025;
Published online: 25 April 2025

References

1. Uoyama, H., Goushi, K., Shizu, K., Nomura, H. & Adachi, C. Highly efficient organic light-emitting diodes from delayed fluorescence. *Nature* **492**, 234–238 (2012).
2. Tao, Y. et al. Thermally activated delayed fluorescence materials towards the breakthrough of organoelectronics. *Adv. Mater.* **26**, 7931–7958 (2014).

3. Kenry, Chen, C. & Liu, B. Enhancing the performance of pure organic room-temperature phosphorescent luminophores. *Nat. Commun.* **10**, 2111 (2019).
4. Wang, X. et al. Organic phosphors with bright triplet excitons for efficient X-ray-excited luminescence. *Nat. Photonics* **15**, 187–192 (2021).
5. Han, Y. et al. Rational design of oxygen-enriched carbon dots with efficient room-temperature phosphorescent properties and high-tech security protection application. *ACS Sustain. Chem. Eng.* **7**, 19918–19924 (2019).
6. Zhang, Y. et al. Organic room-temperature phosphorescence materials for bioimaging. *Chem. Commun.* **59**, 5329–5342 (2023).
7. Jiang, P., Liu, Y., Ding, B. & Ma, X. Regulation strategies of dynamic organic room-temperature phosphorescence materials. *Chem. Bio Eng.* **1**, 13–25 (2024).
8. Wu, H. et al. Molecular phosphorescence in polymer matrix with reversible sensitivity. *ACS Appl. Mater. Interfaces* **12**, 20765–20774 (2020).
9. Liang, Z. et al. Activating molecular room-temperature phosphorescence by manipulating excited-state energy levels in poly(vinyl alcohol) Matrix. *ACS Appl. Mater. Interfaces* **15**, 35534–35542 (2023).
10. Totani, K., Okada, Y., Hirata, S., Vacha, M. & Watanabe, T. Thermoresponsive persistent phosphorescent color change using efficient thermally activated reverse energy transfer with a large energy difference. *Adv. Opt. Mater.* **1**, 283–288 (2013).
11. Chi, Y. & Chou, P.-T. Transition-metal phosphors with cyclometalating ligands: fundamentals and applications. *Chem. Soc. Rev.* **39**, 638–655 (2010).
12. Ulbricht, C., Beyer, B., Friebe, C., Winter, A. & Schubert, U. S. Recent developments in the application of Phosphorescent Iridium(III) complex systems. *Adv. Mater.* **21**, 4418–4441 (2009).
13. You, Y. & Park, S. Y. Phosphorescent iridium(iii) complexes: toward high phosphorescence quantum efficiency through ligand control. *Dalton Trans.* 1267–1282 https://doi.org/10.1039/B812281D (2009).
14. Yan, J. et al. Electroluminescence and hyperphosphorescence from stable blue Ir(III) carbene complexes with suppressed efficiency roll-off. *Nat. Commun.* **14**, 6419 (2023).
15. Liu, Y., Yiu, S.-C., Ho, C.-L. & Wong, W.-Y. Recent advances in copper complexes for electrical/light energy conversion. *Coord. Chem. Rev.* **375**, 514–557 (2018).
16. Li, K. et al. Highly phosphorescent platinum(II) emitters: photophysics, materials and biological applications. *Chem. Sci.* **7**, 1653–1673 (2016).
17. Cebrián, C. & Mauro, M. Recent advances in phosphorescent platinum complexes for organic light-emitting diodes. *Beilstein J. Org. Chem.* **14**, 1459–1481 (2018).
18. Hamzehpoor, E. et al. Efficient room-temperature phosphorescence of covalent organic frameworks through covalent halogen doping. *Nat. Chem.* **15**, 83–90 (2023).
19. Fateminia, S. M. A. et al. Organic nanocrystals with bright red persistent room-temperature phosphorescence for biological applications. *Angew. Chem. Int. Ed.* **56**, 12160–12164 (2017).
20. Li, J. et al. Unexpected long room-temperature phosphorescence lifetimes of up to 1.0 s observed in iodinated molecular systems. *Chem. Commun.* **57**, 8794–8797 (2021).
21. Mieno, H., Kabe, R. & Adachi, C. Reversible control of triplet dynamics in metal-organic framework-entrapped organic emitters via external gases. *Commun. Chem.* **1**, 27 (2018).
22. Mukherjee, S. & Thilagar, P. Recent advances in purely organic phosphorescent materials. *Chem. Commun.* **51**, 10988–11003 (2015).
23. Lewis, G. N. & Kasha, M. Phosphorescence and the Triplet State. *J. Am. Chem. Soc.* **66**, 2100–2116 (1944).
24. Zhang, Z. et al. A synergistic enhancement strategy for realizing ultralong and efficient room-temperature phosphorescence. *Angew. Chem. Int. Ed.* **59**, 18748–18754 (2020).
25. Chen, C. et al. Carbazole isomers induce ultralong organic phosphorescence. *Nat. Mater.* **20**, 175–180 (2021).
26. Nie, X. et al. Aromatic electrophilic directing for fluorescence and room-temperature phosphorescence modulation. *J. Phys. Chem. Lett.* **12**, 3099–3105 (2021).
27. Jena, S. et al. Crystallization induced room-temperature phosphorescence and chiral photoluminescence properties of phosphoramides. *Chem. Sci.* **13**, 5893–5901 (2022).
28. Jena, S. et al. Modulating the room temperature phosphorescence by tweaking SOC and P = X Interactions (X = O, S, and Se) in Phosphoramides: Magnetic circularly polarized luminescence from achiral phosphoramides. *Adv. Opt. Mater.* **11**, 2300923 (2023).
29. Ding, B., Ma, X. & Tian, H. Recent advances of pure organic room temperature phosphorescence based on functional polymers. *Acc. Mater. Res.* **4**, 827–838 (2023).
30. Li, Q. et al. Induction of long-lived room temperature phosphorescence of carbon dots by water in hydrogen-bonded matrices. *Nat. Commun.* **9**, 734 (2018).
31. Wu, Z., Nitsch, J. & Marder, T. B. Persistent room-temperature phosphorescence from purely organic molecules and multi-component systems. *Adv. Opt. Mater.* **9**, 2100411 (2021).
32. Qian, C. et al. More than Carbazole derivatives activate room temperature ultralong organic phosphorescence of Benzoindole derivatives. *Adv. Mater.* **34**, 2200544 (2022).
33. Cao, P., Chen, Q. & Wu, P. Boric Acid Matrix-Activated $n\pi^*$ transition of guest chromophores: from pure fluorescence to efficient afterglow. *Adv. Opt. Mater.* **12**, 2401399 (2024).
34. Yang, J. et al. The influence of the molecular packing on the room temperature phosphorescence of purely organic luminogens. *Nat. Commun.* **9**, 840 (2018).
35. Wang, Z. et al. Regulation of irradiation-dependent long-lived room temperature phosphorescence by controlling molecular structures of chromophores and matrix. *Adv. Opt. Mater.* **10**, 2200481 (2022).
36. Zhu, Y., Wang, X. & Wu, M. Intriguing room temperature phosphorescence in crystalline porous organic frameworks. *Adv. Funct. Mater.* **33**, 2308096 (2023).
37. Guo, J., Yang, C. & Zhao, Y. Long-lived organic room-temperature phosphorescence from amorphous polymer systems. *Acc. Chem. Res.* **55**, 1160–1170 (2022).
38. Horie, K. & Mita, I. Photochemistry in polymer solids. Decay of benzophenone phosphorescence in poly(methyl methacrylate). *Chem. Phys. Lett.* **93**, 61–65 (1982).
39. Horie, K., Morishita, K. & Mita, I. Photochemistry in polymer solids. 3. Kinetics for nonexponential decay of benzophenone phosphorescence in acrylic and methacrylic polymers. *Macromolecules* **17**, 1746–1750 (1984).
40. Muhammed Munthasir, A. T. et al. Quadrupling the PLQY of Tetraphenylethylene by covalently linking it with isosteric tetraarylaminoborane: a potential candidate for multicolor live cell imaging. *Inorg. Chem*. acs.inorgchem.4c04036 https://doi.org/10.1021/acs.inorgchem.4c04036 (2025).
41. Yu, Y. et al. π-Extended Heli(aminoborane)s with highly bright circularly polarized luminescence and narrowband emission. *Angew. Chem. Int. Ed*. e202501645 https://doi.org/10.1002/anie.202501645 (2025).
42. El-Sayed, M. A. Spin—orbit coupling and the radiationless processes in nitrogen heterocyclics. *J. Chem. Phys.* **38**, 2834–2838 (1963).
43. Xu, L. et al. Tunable ultralong organic phosphorescence modulated by main-group elements with different Lewis acidity and basicity. *J. Mater. Chem. C.* **8**, 14740–14747 (2020).

44. Ganesan, P. et al. Methoxy substituents activated carbazole-based boron dimesityl TADF emitters. *J. Mater. Chem. C.* **8**, 4780–4788 (2020).
45. Lien, Y.-J. et al. First N-borylated emitters displaying highly efficient thermally activated delayed fluorescence and high-performance OLEDs. *ACS Appl. Mater. Interfaces* **9**, 27090–27101 (2017).
46. Nandi, R. P., Kalluvettukuzhy, N. K., Pagidi, S. & Thilagar, P. Molecular persistent room-temperature phosphorescence from Tetraarylaminoboranes. *Inorg. Chem.* **62**, 1122–1134 (2023).
47. Kalluvettukuzhy, N. K. et al. Chiral B–N AIEgens: Intense blue circularly polarized luminescence and piezochromism. *Org. Lett.* **25**, 6067–6071 (2023).
48. Liu, J. et al. Circularly polarized organic ultralong room-temperature phosphorescence with a high dissymmetry factor in chiral helical superstructures. *Adv. Mater.* **36**, 2306834 (2024).
49. Patil, Y., Demangeat, C. & Favereau, L. Recent advances in room temperature phosphorescence of chiral organic materials. *Chirality* **35**, 390–410 (2023).
50. Lin, Z. et al. Employing racemization strategies to simultaneously enhance the quantum yield, lifetime, and water stability of room-temperature phosphorescent materials. *Chem. Sci.* **15**, 8052–8061 (2024).
51. Jung, H. S., Yun, T., Cho, Y. & Jeon, H. B. Simple and convenient copper-catalyzed amination of aryl halides to primary arylamines using NH4OH. *Tetrahedron* **72**, 5988–5993 (2016).
52. Neena, K. K. & Thilagar, P. Replacing the non-polarized C=C bond with an isoelectronic polarized B–N unit for the design and development of smart materials. *J. Mater. Chem. C.* **4**, 11465–11473 (2016).
53. Glogowski, M. E., Grisdale, P. J., Williams, J. L. R. & Regan, T. H. Boron photochemistry. *J. Organomet. Chem.* **54**, 51–60 (1973).
54. Glogowski, M. E., Grisdale, P. J., Williams, J. L. R. & Costa, L. Boron photochemistry. *J. Organomet. Chem.* **74**, 175–183 (1974).
55. Pavia, D. L., Lampman, G. M. & Kriz, G. S. Ultraviolet Spectroscopy. in *Introduction to Spectroscopy* 680 (Thomson Brooks/Cole, 2001).
56. Cancès, E. & Mennucci, B. New applications of integral equations methods for solvation continuum models: ionic solutions and liquid crystals. *J. Math. Chem.* **23**, 309–326 (1998).
57. Appiarius, Y. et al. Boosting quantum yields and circularly polarized luminescence of penta- and hexahelicenes by doping with two BN-groups. *Chem. Sci.* **15**, 466–476 (2024).
58. Di Bari, L., Pescitelli, G., Marchetti, F. & Salvadori, P. Anomalous CD/UV Exciton Splitting of a Binaphthyl Derivative: The Case of 2,2‘-Diiodo-1,1‘-binaphthalene. *J. Am. Chem. Soc.* **122**, 6395–6398 (2000).
59. Padalkar, V. S., Patil, V. S. & Sekar, N. Synthesis and characterization of novel 2, 2’-bipyrimidine fluorescent derivative for protein binding. *Chem. Cent. J.* **5**, 72 (2011).
60. Jena, S. et al. Single molecular persistent room-temperature phosphorescence and circularly polarized luminescence from binaphthol-decorated optically innocent Cyclotriphosphazenes. *Chem. – Eur. J.* **29**, e202301924 (2023).
61. Gu, L. et al. Circularly polarized organic room temperature phosphorescence from amorphous copolymers. *J. Am. Chem. Soc.* **143**, 18527–18535 (2021).

Acknowledgements

J.E. and S.G. (IISc) acknowledge support from the Prime Minister’s Research Fellowship (PMRF), India. A.C. thanks IISER Tirupati for the doctoral fellowship. S.G. (UniTS) and N.H. thank the Ministero dell’università e della ricercar (MUR) for financial support through the PRIN project 20227YNHEB; and the staff of the XRD1 beamline for their technical assistance. J.K. acknowledges financial support from STARS, MoE, Government of India (Project ID: 2023-0490). P.T. is thankful to the Science and Engineering Research Board (SERB) (New Delhi, India) and IISc for the financial support. J.E. sincerely thanks Dr. Neena K.K. for her valuable suggestions.

Author contributions

The manuscript was written through contributions from all authors. J.E. conducted the compound synthesis, characterizations, photophysical studies, preliminary DFT studies, demonstration of application and data analysis. S.G. (IISc) contributed to the theoretical calculations, application and data analysis. S.G. (UniTS) and N.H. performed the single crystal X-ray diffraction studies and structure analysis. A.C. and J.K carried out the CPL studies. P.T. organized the entire project, J.E. wrote the manuscript as directed by P.T. All the authors commented on the manuscript and approved the final version.

Competing interests

The authors declare no competing interests.

Additional information

Supplementary information The online version contains supplementary material available at https://doi.org/10.1038/s42004-025-01529-8.

Correspondence and requests for materials should be addressed to Jatish Kumar, Neal Hickey or Pakkirisamy Thilagar.

Peer review information *Communications Chemistry* thanks Yanhua Cheng and the other, anonymous, reviewers for their contribution to the peer review of this work. Peer review reports are available.